Experiment and method of maize ear threshing under airflow mixed impact

Yanan Li, Xinping Li*, Jiarui Hou, Junyi Wang, Bin Peng, Ruizhe Sun

(*College of Agricultural Equipment Engineering, Henan University of Science and Technology, Luoyang 471003, Henan, China*)

Abstract: This study addresses the high breakage rates in the traditional mechanical processing of maize kernels. This paper examines force transfer and consumption within longitudinal and transverse force chain networks by integrating high-speed low-flow and low-speed high-flow methodologies. A mathematical model was developed, incorporating the concept of contact force. Using factors such as airflow impact angle, direction, and regions of maize ears as test variables, three-dimensional force values and threshing quantities were analyzed as key performance indicators. The investigation explored the relationship between three-dimensional forces, destructive forces, and these test factors while examining changes in primary impact forces. High-speed photography was employed to validate the established threshing rules and trajectories. Results indicated that contact forces among different regions of a maize ear were approximately equal. Under specified conditions, transverse threshing was more efficient than longitudinal threshing. The magnitude of the three-dimensional forces followed the order of *Z*-direction > *Y*-direction > *X*-direction, indicating that the predominant impact occurs primarily along the *Z*-axis. For the force values in each direction and region, the large sections exhibited the highest forces, followed by the middle sections, while the small sections displayed the lowest overall forces. Additionally, longitudinal three-dimensional force values exceeded those measured transversely. The destructive force resulting from longitudinal chain network fractures was greater than that from transverse chain network fractures. Furthermore, within each region, the destructive force was inversely proportional to the number of threshing rows. In contrast, across different regions, this value was positively correlated with the number of threshing rows. The rate of change in force values within each region directly correlated with the impact angle. High-speed photography revealed that the transverse threshing process follows a spiral trajectory, whereas the longitudinal threshing trajectory aligns with the axial direction. The movement trajectories of maize kernels are all similar to parabolic movements. This study fills a gap in the study of airflow threshing for high water-content maize.

Keywords: high velocity airflow, low velocity airflow, coupling, impact, maize threshing

DOI: 10.25165/j.ijabe.20261901.9611

Citation: Li Y N, Li X P, Hou J R, Wang J Y, Peng B, Sun R Z. Experiment and method of maize ear threshing under airflow mixed impact. Int J Agric & Biol Eng, 2026; 19(1): 11–20.

1 Introduction

Maize is widely cultivated worldwide and is a major food crop with important economic value[1]. With the continuous increase of planting area, higher requirements are put forward for maize threshing quality, which is significant to world food security[2-4]. Maize threshing is an important step in agricultural harvest. Reducing the rate of kernel breakage and increasing the rate of maize threshing will promote agricultural harvest and industrial development[5-8]. However, the high loss rate of the kernel and the exploration of low-loss methods have become one of the main factors restricting its development[9-13]. Therefore, it is essential to promote the application of maize threshing technology further.

At present, the main method of threshing maize kernels is mechanical threshing. Threshing principles include impact, friction, brushing, and grinding, which will cause certain damage to maize kernels[14-17]. Although air threshing is currently at a blank stage in this field, airflow has already made corresponding developments in the agricultural field. For example, Zhang et al.[7] explored the effects of air supply distance, fan battle speed, and blade number on the airflow field in clean rooms through the working parameters of centrifugal fans. It was found that the combined experiment of fan and cleaning screen could greatly reduce the loss rate and impurity rate of maize. Wang et al.[18] took two varieties of maize in East China as the research object, carried out hot air drying on different initial water content and drying temperatures, and analyzed the starch structure and physical and chemical structure of maize kernels. It was found that the physicochemical and structural characteristics of starch of the two varieties were significantly affected by the interaction of initial water content and heating temperature. Ghafori et al.[19] adopted a suction pneumatic conveying system to explore the physical and conveying characteristics of maize and barley. They found that with the increase in airspeed, the mechanical damage of the two kinds of seeds increased linearly. Under the control of conveying speed, seeds' specific energy consumption and mechanical damage could be significantly reduced. Zhang et al.[20] determined the type of hole number, hole diameter, advance speed, and working negative pressure of the seed tray and seed disturbance tooth by disturbing

Received date: 2024-12-17 **Accepted date:** 2025-12-09

Biographies: Yanan Li, PhD candidate, research interest: new institution, theory of agricultural machinery, Email: LI1516359758@126.com; **Jiarui Hou**, MS candidate, research interest: agricultural machinery and intelligent equipment, Email: rjdj888813@163.com; **Junyi Wang**, MS candidate, research interest: agricultural machinery and intelligent equipment, Email: 15139042158@163.com; **Bin Peng**, MS candidate, research interest: agricultural machinery and intelligent equipment, Email: 220320261824@stu.haust.edu.cn; **Ruizhe Sun**, MS candidate, research interest: agricultural machinery and intelligent equipment, Email: 18639156721@163.com.

***Corresponding author: Xinping Li**, Professor, research interest: agricultural products processing and harvesting machinery. College of Agricultural Equipment Engineering, Henan University of Science and Technology, Luoyang 471003, China. Tel: +86-13592065522, Email: aaalxp@163.com.

the garlic seed metering device with fluid dynamics simulation. They found that the seeding rate and leakage rate could be significantly improved. However, there is a lack of understanding of the research mechanism of the airflow in the discrete threshing of seeds and other aspects[9,21-24].

This study addresses the underexplored field of airflow threshing for high water-content maize by investigating the mechanical properties and dispersion effects of high-speed low-flow and low-speed high-flow coupling on kernels. Based on the arrangement units of maize sets, circulating force circle, and the cooperative carrying capacity of maize kernels, we analyzed the transmission and consumption processes within the longitudinal and transverse force chain network of maize ears under air coupling. Furthermore, the effects of the three-dimensional force value and destructive value on test factors and indices were explored. This work provides a reference for applying air coupling to high water-content maize kernels.

2 Analysis of basic characteristics of maize ear

2.1 Analysis of mechanical characteristics of maize ear

Conventional maize threshing primarily relies on mechanical methods, which separate kernels through impact, rubbing, and extrusion. However, these traditional techniques cause substantial damage to seed maize, which differs significantly from commercial maize[25-27]. In contrast, a novel approach coupling high-speed and low-speed airflow offers a cleaner, more environmentally friendly alternative with low damage and sustained airflow efficacy[28,29].

The ears of maize are approximately cylindrical, and the research group found that the maize kernels follow the "ABA" principle of staggered joints and lapping, calling this law of maize combination "arrangement unit"[30-33]. In every two rows of the maize ears, the longitudinal kernels are in direct contact with the transverse ones to form opposing gaps A, while the transverse and longitudinal kernels are in staggered contact to form interlaced gaps B. ABA staggered overlap is formed on the entire maize ear. The transverse kernels follow the 11-22 staggered overlap principle, that is, the sides of the two transverse maize kernels in a single layer are in direct contact to form a 1-1 contact, and then the sides of the two transverse kernels in the other two layers, which are also in 1-1 contact, are in staggered contact to form the 11-22 staggered overlap principle. As shown in Figure 1.

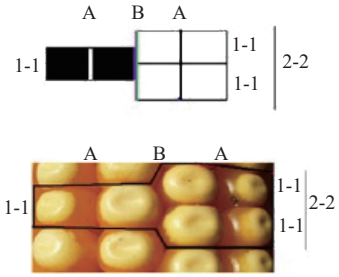

Figure 1 Maize arrangement unit is overlapped with the staggered joint

2.2 Radial force analysis and longitudinal force chain balance of maize kernels

Upon impact by the coupled airflow, the force F is partially applied directly to the kernel surface, with the remainder transmitted along the kernel due to lateral squeezing. This impact force F is subsequently decomposed: one portion is transmitted toward the maize cob as F_D, while the other is transferred to adjacent kernels as a lateral squeezing force F_S. The transmission process of this airflow impact force is shown in Figure 2a.

During airflow impact threshing, maize kernels are regarded as flat plates with upper and lower surfaces. The impact, combined with the squeezing effect from surrounding kernels, induces an oblique motion in each kernel. Consequently, the threshing process is characterized as movement along an inclined plane, with the kernels experiencing both lift and drag forces within the airflow. The area of the lateral contact plane of the kernels can be set as S, and the flow velocity in the impact area of the airflow, which impacts the kernels, is v, directed upward obliquely. The angle between the maize kernels and the plane where the tangent is located is τ, and the velocity can be decomposed into the horizontal direction and the vertical direction. The horizontal velocity is $v_x = v\cos\tau$, and the vertical velocity is $v_y = v\sin\tau$, as shown in Figure 2b. Then the upper surface of the maize kernels will be subjected to normal resistance, and the total normal resistance is:

$$F_n = \frac{3}{2}\rho s v_x^2 \sin^2\tau = \frac{3}{2}\rho s v^2 \cos\tau^2 \sin^2\tau \quad (1)$$

where, v is the flow rate of the impact area, m/s; ρ is the density of air, kg/m^3; s is the contact area, m^2.

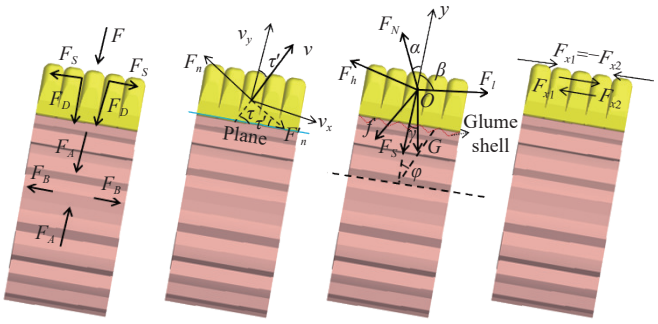

a. Transmission of force b. Air lift c. Radial force analysis d. Longitudinal force analysis

Note: τ is the angle between the direction of kernel movement and the tangential horizontal plane; α is the angle between the supporting force and the Y-axis; ε is the angle between maize extrusion pressure on both sides and the axis; β is the angle between the coupled airflow and the Y-axis; γ is the angle between gravity and the Y-axis; F_N is the supporting force of glume shell on kernel when angle is α; f is the friction force of the glume shell on the kernel at the angle; F_h, F_l are the extrusion pressure of the misaligned lap; F_z is the impact force of the airflow in the impact area; G is kernel gravity; F_s is the connection force between the kernel and the carpopodium of the maize; F_{x1}, F_{x2} are longitudinal forces.

Figure 2 Stress analysis of maize kernels

When maize kernels move obliquely upward, the surface of the kernels is affected by air resistance. The angle between the upper surface and the tangent line is τ'. Then $\tau' = \frac{\pi}{2} - \tau$, is perpendicular to the upper surface, and the lower surface is equal to the upper surface, the direction opposite. Then the resistance on the upper surface is:

$$F_n' = \frac{3}{2}\rho s v_y^2 \sin^2\tau' = \frac{3}{2}\rho s (v\sin\tau)^2 \sin^2\left(\frac{\pi}{2} - \tau\right) = \frac{3}{2}\rho s v^2 \sin^2\tau\cos\tau^2 \quad (2)$$

The component of the normal force F_n' on X-axis is:

$$F = -F_n' \sin\tau = -\frac{3}{2}\rho s v^2 \sin^3\tau\cos^2\tau \quad (3)$$

Projection to the vertical direction and then downward, negative, so the vertical component of the normal resistance of the upper surface is:

$$F' = -F'_n \cos\tau = -\frac{3}{2}\rho s v^2 \sin^2\tau \cos^2\tau \tag{4}$$

According to Figure 2c, the radial force under external force conditions can be obtained by analyzing the force of airflow on maize kernels:

$$F_y = (F_h + F_l)\cos\beta + \int_{\alpha_1}^{\alpha_2} F_{N\alpha}\cos\alpha d\alpha - \int_{\alpha_1}^{\alpha_2} f_\alpha |\cos\alpha| d\alpha - G\cos\gamma - F_S - \frac{3}{2}\rho s v \sin^2\tau\cos^2\tau = 0 \tag{5}$$

There are longitudinal force chains between maize kernels, which are mainly balanced by the extrusion pressure of both sides of the kernels, the friction force of the dislocated overlapping kernels, the carpopodium connection, and the contact force.

When the airflow is blown longitudinally towards the kernels for dispersion, the radial force and the lateral force are zero at this time, and the longitudinal force chain equilibrium is shown in Figure 2d. According to the kernel arrangement rules, there is a contact force between maize kernels (the definition and calculation of contact force are shown in 2.3). A single kernel has five contact surfaces. The contact surface areas are regarded as approximately equal, while the glume shell support force is relatively small and can be ignored. The reason is that, based on the inherent biological characteristics of the maize cob, the maize kernels are mainly connected by the carpopodium and the maize cob, and the glumes are the parts surrounding the maize carpopodium, providing relatively little support to the maize kernels. Then the calculation formula for the contact force F_c can be derived as:

$$F_c = \frac{F_{si} - F_{mi}}{5\mu} \tag{6}$$

where, μ is the friction coefficient between maize kernels; F_{si} is complete maize carpopodium force, N; F_{mi} is the carpopodium force of maize single kernel, N.

The longitudinal force of the maize kernels is as follows:

$$F_x = 5nF_c - (n-1)F_c + nF_s\tan\delta = (4n+1)F_c + nF_s\tan\delta \tag{7}$$

where, n is the number of contacts of maize kernels in the direction of external force; δ is the angle between adjacent kernels, (°).

The force chain fracture condition under the action of external forces is:

$$F_z \sin\beta \geq (4n+1)F_c + nF_s\tan\delta \tag{8}$$

From the above stem force F_s and contact force F_c, we can see:

$$F_z \geq \frac{(4n+1)F_c + nF_s\tan\delta}{\sin\beta} \tag{9}$$

where, β is the angle between the airflow and the kernel, (°); F_z is the force of air coupling blowing to the kernel, N; F_s is the maximum carpopodium strength between maize kernels, N; F_c is the contact force between maize kernels, N.

2.3 Transverse force chain network transmission and consumption process

Experimental and prior research by our group indicates that a maize ear is composed of misaligned arrangement units, as shown in Figure 1. Beyond the radial force chain, a transverse force chain exists, formed by these units along an axial helix to create a closed loop. The transverse trapezoid transfer and relative trapezoid transfer within this structure mutually cancel. However, when the misaligned arrangement units are subjected to lateral external forces, this chain is readily disrupted. The transfer process of this force chain network is depicted in Figure 3.

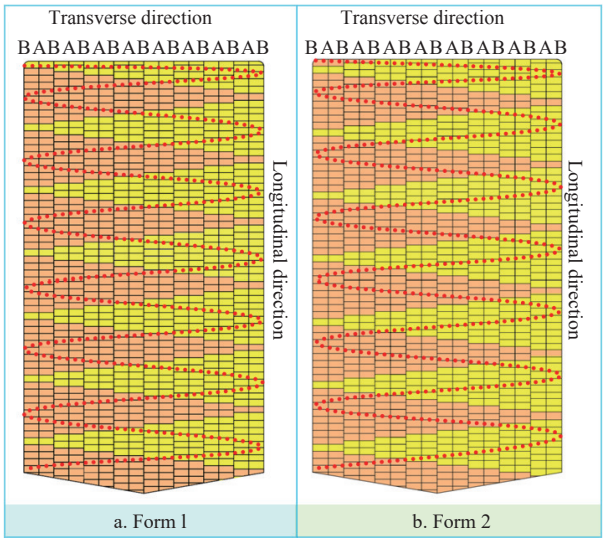

Figure 3 Force chain network of the lateral bond unit

Figure 1 shows that the mutual squeezing and misalignment of maize kernels form force chains organized into arrangement units. When airflow impacts the maize, the resulting force F_1 is transmitted along the kernels and laterally through these arrangement units. Due to the fact that the side-by-side kernels are interlaced with the other two kernels, the force F_1 is transmitted to $F_{3,4}$ and $F_{3,5}$. During this process, F_1 gradually diverts. Assuming the carpopodium connection force and frictional force of a single kernel are identical, the force on each subsequent pair of misaligned and overlapped kernels during transmission is halved, as shown in Figure 4a. The resulting force chain network transmission is depicted in Figure 4b.

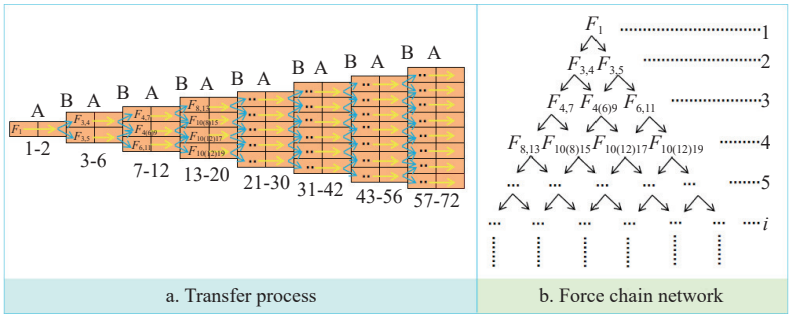

Figure 4 Transverse transfer and consumption process of force chain ladder form

For example, $F_{4(6)7}$ is the overlapping force of the diverging forces F_{47} and F_{67}. The surface of maize is arc-shaped, and there is an angle φ between the misaligned arrangement units. Therefore, in an ideal state, the discrete kernel peeling formula of column i is

derived as follows:

$$F_1 = (F_{3,4} + F_{3,5})\cos\varphi = (F_{4,7} + F_{4(6)9} + F_{6,11})\cos\varphi = \ldots\ldots = \sum_{i=1}^{n} F_i \cos\varphi \tag{10}$$

where, F_i is the air force, N; φ is the angle between the misalignment of the arrangement units, (°); and i is the column where the seeds are located.

From Figures 1 and 3, it can be seen that the kernels are superimposed. Therefore, the force condition of a single kernel in the threshing area is:

$$F_e = \begin{cases} \dfrac{1}{2^{i-1}} F_i \cos\varphi, & i \le 2 \\ \dfrac{1}{2^{i-2}} F_i \cos\varphi, & i > 2 \end{cases} \tag{11}$$

In force transfer, when $i > 2$, the superimposed single-kernel force is regarded as the force transferred by the previous kernel in the threshing region.

If F'_1, which is the force on the kernel under the action of the actual airflow, also includes the supporting force of the glume shell, the gravity of the maize ear, and the connection force of the carpopodium, etc., then the equilibrium condition is:

$$F_e \ge F'_1 \tag{12}$$

Similarly, in the threshing process, only the arrangement unit force in the impact area is most likely to break the closing force chain, so as long as the threshing conditions of a row of kernels in the threshing area are met, discrete threshing can be realized. Then, the closure force chain break of the threshing region and threshing conditions are:

$$F_e \le F'_1 \tag{13}$$

Therefore:

$$F'_1 \ge \begin{cases} \dfrac{1}{2^{i-1}} F_i \cos\varphi, & i \le 2 \\ \dfrac{1}{2^{i-2}} F_i \cos\varphi, & i > 2 \end{cases} \tag{14}$$

3 Materials and methods

3.1 Test materials and equipment

The experiment utilized the maize variety Boyun 88, selected for being moth-free, disease-free, and uniformly sized. After uniform drying, the ears were controlled to the same moisture classification, with no significant difference in water content among them. As measured following GB/T3543.6, the mean water content ranged from 25.8%-27.5%.

The main test equipment is JHBM-H5, JHBL-3 sensor, four-way digital signal converter, USB-to-serial port converter, and mechanical test software produced by Bengbu Jinnuo Sensor Co., LTD. The equipment also includes the TA.XTC-16 texture analyzer; JNY-20A air compressor, used for gas compression, to provide power for air threshing; XGB-2200 high-pressure vortex fan to provide auxiliary power for air threshing and compensate for lost airflow; AS836 digital anemometer for measuring airflow velocity 1; and the American Phantom Miro series LC111 high-speed digital camera, resolution 1 280 800, maximum shooting rate 400 000 fps, sensitivity ISO-12 232 SAT, minimum exposure time 2. The electronic angle ruler is used to measure the angle between the maize and the flow tube (the angle between the transverse tangent line and the flow tube axis and the angle between the longitudinal axis and the flow tube axis). Combined with the above test equipment, a three-dimensional force measuring device for maize ear with air coupling impact was developed, as shown in Figure 5.

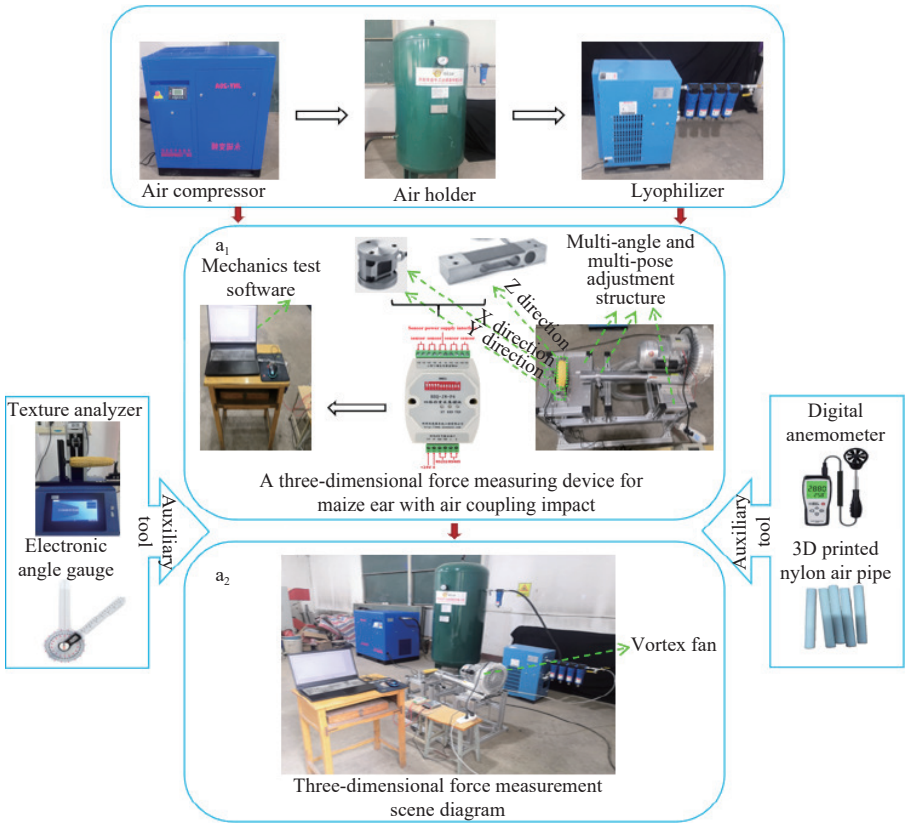

Figure 5 Three-dimensional force measuring device for maize ear with air coupling impact

3.2 Measurement of contact force between maize kernels

Longitudinal and transverse equilibrium force chains exist within the maize kernels. The closure of the transverse chain and the balance of the longitudinal chain are maintained by the contact extrusion force between kernels, defined here as the contact force.

For the tensile test, the texture analyzer was set to a speed of 2 mm/s. A hot melt glue stick was heated, applied to secure the sample, and then stretched to collect data. Tests were performed on both the entire maize ear and on individual kernels from large, middle, and small sections, as shown in Figure 6.

Fifty maize ears were selected and divided into four groups. Each group was tested three times to obtain the average value. Table 1 shows the carpopodium force measurement in different regions.

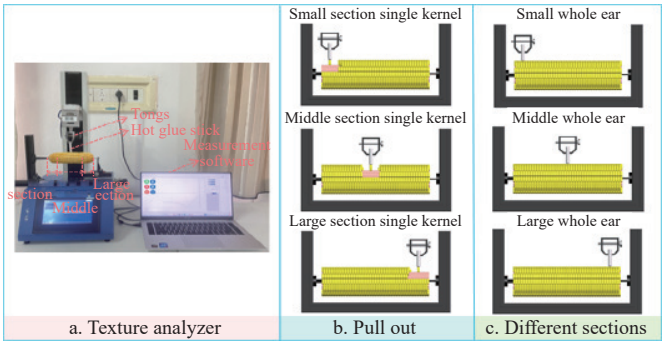

Figure 6 Drawing a diagram of each region of maize ear

Table 1 Carpopodium force measurement

Type	Region	Experimental group number				Average carpopodium force
		1	2	3	4	
Carpopodium force of whole maize ears F_{si}/N	Large section	11.40	10.012	11.019	11.219	10.913
	Middle section	8.616	8.217	9.765	11.967	9.6413
	Small section	7.302	8.664	7.330	7.215	7.628
Carpopodium force of individual maize kernels F_{mi}/N	Large section	10.291	9.370	8.941	10.101	9.676
	Middle section	7.591	8.103	9.040	9.129	8.466
	Small section	6.091	7.491	6.504	6.139	6.556

Table 1 shows the analysis of the carpopodium force of whole maize and single kernel. The average carpopodium force on whole maize was F_{s1}=10.913 N, F_{s2} =9.6413 N, F_{s3} =7.628 N; the average carpopodium force of a single kernel was F_{m1} =9.676 N, F_{m2} =8.466 N, and F_{m3} =6.556 N. The contact force was calculated by Equation (6), and the static friction coefficient between kernels was 0.32[34]; then the contact force G was 0.713 N, 0.735 N, and 0.67 N, respectively. Thus the difference between the contact forces was not much and can be regarded as approximately equal. The average value of the contact force was 0.706 N.

Force measurement

A maize ear was clamped on a custom 3D force device, with sensors along the X- (tangential), Y- (axial), and Z- (vertical) axes measuring impact forces near its surface. The system used a coupled air duct from a vortex fan (70 mm diameter) and an air compressor (8 mm pipe diameter). Experiments determined the optimal parameters: compressor velocity at 28-32 m/s, vortex fan velocity of 8-12 m/s, and a 14°-16° angle between the compressor tube and fan outlet. Given the system's complexity, key parameters were fixed: an air compressor flow velocity of 30 m/s, a vortex fan flow velocity of 10 m/s, and a 15° angle between the airflow pipe and the vortex fan. A multi-angle structure adjusted the coupled airflow's impact angle, while a clamping device repositioned the maize ear in lateral, longitudinal, and other 3D directions for regional impact. The resulting sensor signals were converted to three-dimensional force data via an AD module. Following calibration with a 500 g weight (<5% error), fifty maize ears were tested. Each group of experiments was repeated three times and the average value was taken.

The coupled impact of airflow would cause damage to both the transverse force chain network and the longitudinal force chain. The longitudinal inter-kernel angle and the dislocation overlap angle between kernels in Figure 7b and Figure 7c were measured as $\delta = 30°$ and $\varphi = 15°$. The initial impact force F measured by the force sensor was 583.1 N.

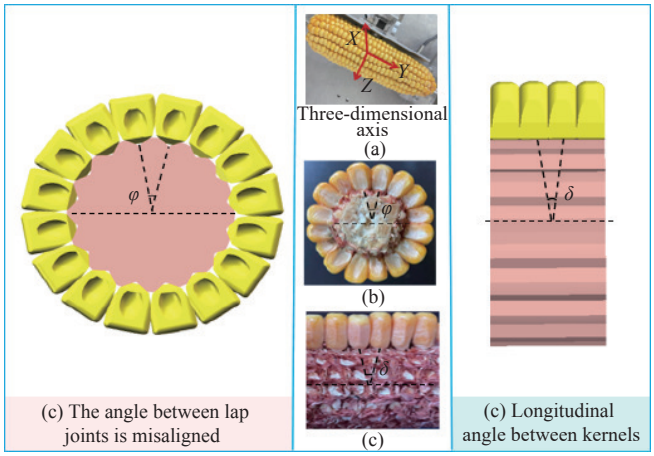

Figure 7 Maize ear three-dimensional coordinates and angle between kernels

The three-dimensional force values under coupled airflow impact were measured, and threshing outcomes in each region were statistically analyzed. The test factors included the airflow impact

Table 2 Force measurements

Direction	Region	Sensor direction	Angle between coupled air flow and maize/(°)				
			75	60	45	30	15
Transverse direction	Large section	X_i	14.542	15.102	11.105	8.546	6.112
		Y_i	4.156	7.101	8.265	6.425	4.478
		Z_i	49.252	31.124	28.186	18.124	13.19
		Number of threshed rows	4	6	5	6	5
		Threshing amount	13	16	20	26	18
		Destructive force F'_{b1}/N	140.819	35.205	70.409	35.205	70.409
	Middle section	X_i	6.368	6.762	8.212	9.5	2.94
		Y_i	6.340	3.146	5.150	8.434	4.579
		Z_i	23.226	13.328	10.118	8.134	12.486
		Number of threshed rows	5	6	5	4	3
		Threshing amount	16	20	17	14	11
		Destructive force F'_{n1}/N	70.409	35.205	70.409	140.819	281.637
	Small section	X_i	6.206	4.514	3.432	3.728	4.120
		Y_i	5.104	2.846	3.138	4.806	4.114
		Z_i	27.134	24.01	12.774	7.180	3.136
		Number of threshed rows	6	5	4	4	2
		Threshing amount	26	18	12	11	4
		Destructive force F'_{l1}/N	35.205	70.409	140.819	140.819	281.637

(To be continued on the next page)

Table 2 (*Continued*)

Direction	Region	Sensor direction	Angle between coupled air flow and maize/(°)				
			75	60	45	30	15
Longitudinal direction	Large section	X_i	5.198	4.538	2.65	2.21	1.470
		Y_i	9.15	9.856	8.390	7.15	5.586
		Z_i	91.83	85.868	67.72	56.644	21.148
		Number of threshed rows	4	4	3	2	0
		Threshing amount	25	22	13	9	0
		Destructive force F_{bz}/N	236.782	232.527	168.711	165.59	2.726
	Middle section	X_i	7.546	5.566	3.724	2.058	4.122
		Y_i	9.514	9.016	8.620	6.742	6.468
		Z_i	67.786	42.178	39.244	24.716	14.308
		Number of threshed rows	4	4	3	3	0
		Threshing amount	22	19	12	10	0
		Destructive force F_{nz}/N	208.455	200.93	155.81	183.832	2.726
	Small section	X_i	5.132	5.816	5.230	4.510	2.646
		Y_i	10.444	8.878	8.522	7.262	5.958
		Z_i	48.098	31.676	27.548	21.168	19.09
		Number of threshed rows	3	5	6	4	0
		Threshing amount	19	25	33	21	0
		Destructive force F_{lz}/N	180.129	264.124	426.731	384.494	2.726

angle (between the coupled airflow and the ear's axis or diameter), ear orientation, and ear region, with the three-dimensional force value and threshing amount as the test indices. Failure modes were analyzed using the longitudinal force chain (Equation (9)), transverse closed force chain (Equation (14)), and Table 1. Force data were acquired and converted by mechanical testing software. The resulting threshing amount, three-dimensional force value, and destructive force per region at various impact angles are summarized in Table 2.

4 Test results and discussion

4.1 Influence of test factors on the threshing quantity

Figure 8 illustrates the effects of the coupled airflow impact angle and maize ear orientation on threshing amounts. The transverse section exhibited a declining trend with increasing angle, while the longitudinal section decreased sharply beyond a critical angle of 45°. In contrast, other regions showed a positive correlation with the impact angle. This is because a larger impact angle concentrates the airflow force, which more readily disrupts the force chain balance. However, the smooth kernel surface promoted airflow passage, consequently reducing the threshing effect. Before reaching the critical airflow value, the force on the longitudinal small section increased gradually. Beyond this point, the force diverged laterally, the impact attenuated, and threshing efficiency declined.

Under the impact angle, the transverse threshing quantity outperformed the longitudinal one in the same area across different ear directions. This was because the longitudinal force chain network was subjected to greater contact force and extrusion pressure from the increased number of stacked kernels. In contrast, for the transverse force chain network, once the impact force broke the "arrangement unit", the surrounding kernels loosened more readily than in longitudinal threshing.

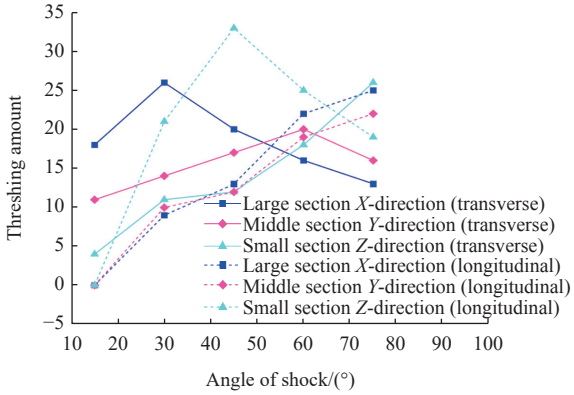

Figure 8 Influence of experimental factors on maize ear threshing amount

4.2 Influence of test factors on the number of displacements

Figure 9 shows the effects of coupled airflow impact angle, maize ear direction, and region on threshing row count. The transverse section remained stable across angles, while the longitudinal section peaked after a critical angle of 45°. Other regions responded proportionally to the angle. Transverse stability is attributed to its large, smooth surface, ensuring stable force transfer. The longitudinal non-monotonic trend resulted from a shift in airflow impact area and distribution at the critical angle, with the initial rise due to increasingly concentrated force.

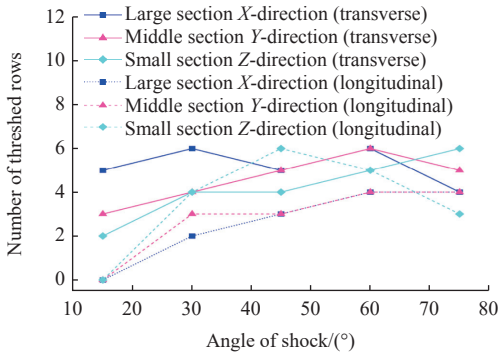

Figure 9 Influence of experimental factors on the number of threshed rows

The results showed that transverse threshing rows increased or stabilized with the impact angle, consistently outperforming longitudinal threshing. In longitudinal threshing, row counts rose in large and middle sections but peaked then declined in small sections. This difference occurred because transverse impact broke the "arrangement unit", progressively collapsing surrounding kernels, whereas longitudinal threshing was influenced by kernel squeezing and uneven airflow distribution over the cylindrical surface.

4.3 Influence of test factors on three-dimensional force value

Figure 10 shows the effects of the coupled impact angle, maize ear direction, and region on the three-dimensional force value. Comparative analysis revealed that the transverse and longitudinal *Z*-direction force values were the greatest in all regions. Furthermore, as the impact angle increased, the force values in each region consistently followed the order of *Z*-direction > *Y*-direction > *X*-direction.

A comparison of force values across regions in the same direction revealed that the large section bore the highest forces, followed by the middle, and then the small section. This distribution occurred because the large section's size and irregular shape

reduced lateral force dispersion, consequently concentrating a greater pulling force on kernels. In contrast, small sections exhibited the opposite effect. The middle section required a larger force in the destructive chain due to its prominent carpopodium connection force.

The longitudinal *Z*-direction and overall three-dimensional force values were greater than their transverse counterparts. This difference is attributed to the distinct force transmission mechanisms: longitudinal airflow diverts to the *X*- and *Z*-directions to directly impact kernels, while transverse impact force is transmitted and consumed along the lateral force chain network, leading to substantial force loss in the *X*- and *Z*-directions.

4.4 Regression analysis of test results

From the above analysis, it can be known that the impact angle has a significant influence on the force value. To further explore the influence of the airflow impact angle on the force value in the *Z*-direction, an analysis of variance was conducted based on the measured data of each group, as listed in Tables 3 and 4.

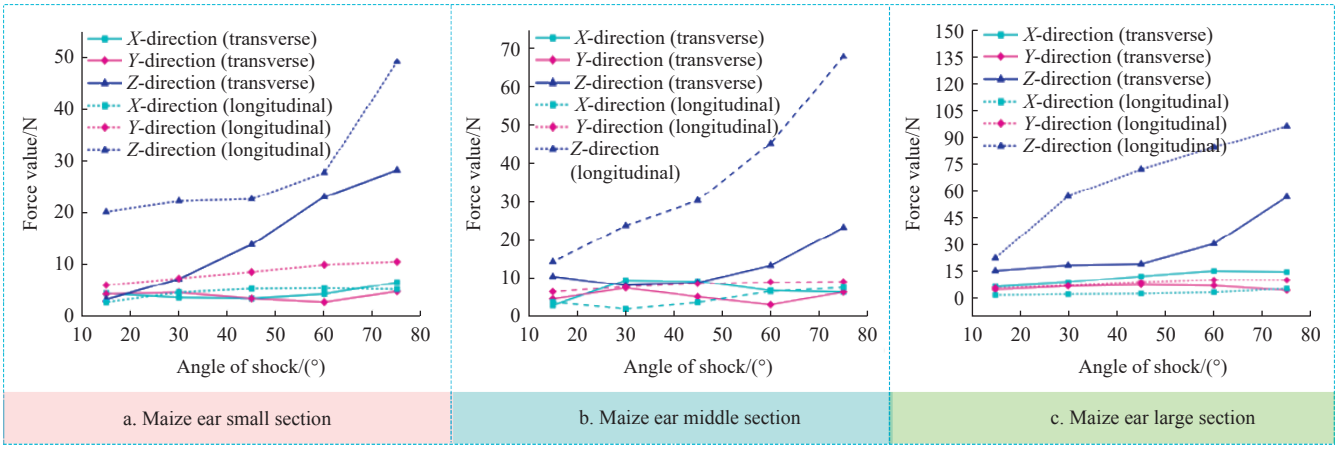

Figure 10 Influence of experimental factors on three-dimensional force value

Table 3 Analysis of variance in the transverse region

Region	Source	Force value in the Z_i-direction				
		DF	SS	MS	*F*	*p*
Transverse large section	Model	5	4021.707	804.341	427.921	<0.001***
	Error	12	22.556	1.879 65		
	Total	17	4044.263			
Transverse middle section	Model	5	736.255	147.251	31.684	<0.001***
	Error	12	55.769	4.647		
	Total	17	792.0243			
Transverse small section	Model	5	1718.077	343.615	103.213	<0.001***
	Error	12	39.95	3.329		
	Total	17	1758.027			

Table 4 Analysis of variance in the longitudinal region

Region	Source	Force value in the Z_i-direction				
		DF	SS	MS	*F*	*p*
Longitudinal large section	Model	5	19 274.752	3854.950	307.386	<0.001***
	Error	12	150.4928	12.541		
	Total	17	19 425.245			
Longitudinal middle section	Model	5	8106.743	1621.349	254.369	<0.001***
	Error	12	76.488	6.374		
	Total	17	8183.231			
Longitudinal small section	Model	5	3489.485	697.897	158.424	<0.001***
	Error	12	52.863	4.405		
	Total	17	3542.348			

Note: * significant (p<0.05); ** relatively significant (p<0.01); *** extremely significant (p<0.001).

As can be seen from Tables 3 and 4, the impact angle has an extremely significant influence on the force value in the *Z*-direction (<0.001), which is the same as the results of the above single-factor analysis.

Using Origin2022 software, curve fitting was performed on the force values in the *Z*-direction to determine the corresponding functional relationship. The regression analysis results are shown in Table 5, and the optimal fitting function is:

$$y_i = Ax^2 + Bx^2 + Cx + D \tag{15}$$

where, y_1 is the three-dimensional force value, N; x is the impact angle of airflow, (°); A, B, C, and D are undetermined coefficients respectively.

It can be seen from Table 5 that the lowest determination coefficient R^2 of the three-dimensional force value regression fitting is 0.9781, indicating that the fitting degree of the above model is relatively high. Therefore, the relationship between the force value in *Z*-direction and the test results can be further explored.

Table 5 Results of regression processing

Direction	Region	Coefficient				
		A	*B*	*C*	*D*	R^2
Transverse	Large section	0.0002	–0.0274	1.3363	–2.0168	0.9781
	Middle section	0.000 01	0.0083	–0.6253	19.826	0.9882
	Small section	–0.0002	0.0334	–0.9433	10.87	0.9895
longitudinal	Large section	0.0003	–0.0573	4.2269	–29.66	0.9883
	Middle section	0.0005	–0.0559	2.7248	–16.252	0.9783
	Small section	0.0002	–0.0182	0.7494	10.988	0.988

4.5 Relationship between destructive force value and test results

The primary determinant of the destructive force is the *Z*-direction force component, which shows a strong dependence on the test factors. As shown in Figure 11a, a distinct contrast was observed: the destructive force of the longitudinal force chain network was markedly greater than that of the transverse network. Moreover, the transverse and longitudinal destructive forces exhibited opposite correlations with the impact angle, being inversely and directly proportional, respectively.

As shown in Figures 11b and 11c, the number of transverse threshing rows was inversely proportional to the destructive force within each region. This relationship arose because force transfer in the transverse force chain network followed a helical, closed-loop

path, where dimensional changes during transfer caused force value overlap. Conversely, the number of longitudinal threshing rows was directly proportional to the destructive force. A greater number of impact rows increased kernel stacking in the airflow direction, thereby raising the destructive force required for chain fracture due to heightened extrusion pressure from surrounding kernels and carpopodium connection force.

The above analysis confirms that the *Z*-direction force value is closely related to the test factors, warranting further investigation into its rate of change. To this end, the variation rate of force values under different ear directions, regions, and impact angles was analyzed using Table 2 and Figure 8. The *Z*-direction force values from each region were selected for curve fitting and subsequent first-order differentiation, as presented in Figure 12.

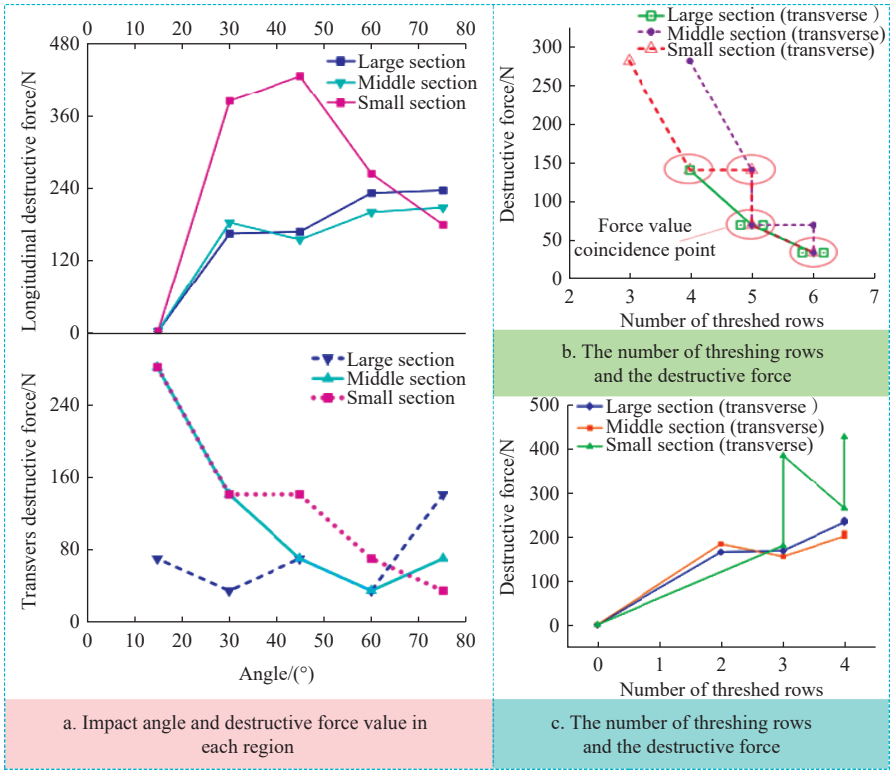

Figure 11 Relation between destructive force value of force chain and test results

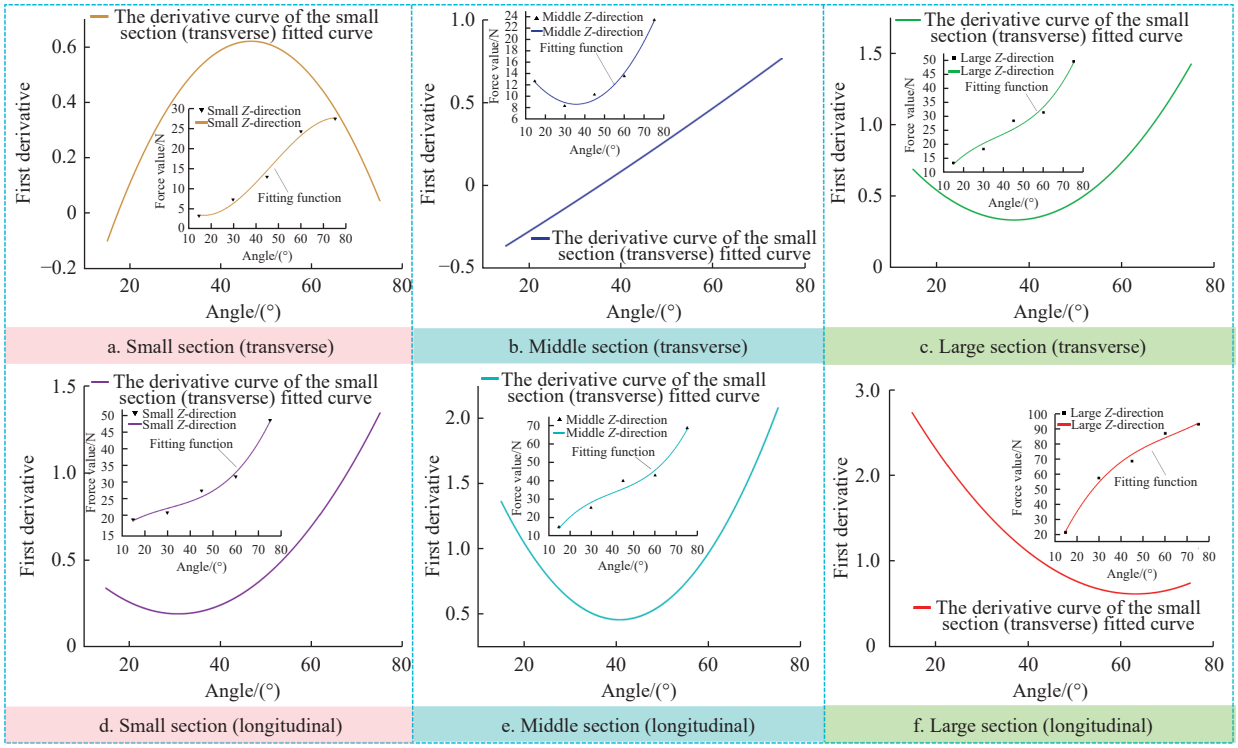

Figure 12 The first derivative of the force value curve

The first derivative of the transverse small section initially increased then decreased, indicating that the force value change rate

accelerated followed by deceleration with increasing angle. Conversely, the longitudinal small section exhibited a decreasing then increasing trend, reflecting a change rate that transitioned from deceleration to acceleration. This divergence arises because the transverse and longitudinal orientations exhibit varied airflow impact areas and velocities under different impact angles in small sections.

The first derivative of the transverse middle section increased continuously, indicating an accelerating rate of force change with the impact angle. In contrast, the longitudinal middle section showed a decreasing then increasing trend, reflecting a change rate that transitioned from deceleration to acceleration. This difference arose because the greater number of longitudinal kernel stacks required a higher destructive force for chain fracture than the transverse direction. Additionally, significant velocity changes occurred during transverse force chain breakage.

For the large transverse section, the first derivative first decreased then increased with the angle, indicating an accelerating rate of force change. Conversely, the derivative for the large longitudinal section decreased, reflecting a decelerating rate. This difference is due to the large kernels' size and irregular arrangement, which caused the transverse airflow to divert and dissipate circumferentially at a significantly higher rate than in the longitudinal direction, leading to its faster change rate.

Analysis of maize threshing rule under lateral 45° high-speed photography

High-speed photography was used to capture the threshing process. For both transverse and longitudinal orientations, sequences of five images were extracted at intervals of 0.925 s, with initial extraction times of 2.295 s and 8.325 s, respectively, as shown in Figure 13.

Analysis of the transverse threshing process via high-speed photography showed that kernel detachment follows a spiral trajectory defined by the "arrangement rule" (Figure 13a). The process initiates when the transverse destructive force surpasses the kernel's force chain strength, causing kernel drop-off and rupture of the "arrangement unit". This rupture breaks the transverse force chain network's closure, thereby allowing the coupled airflow to propagate threshing sequentially along the network in a spiral path.

The longitudinal threshing process proceeded along the axial direction of the balance force chain, as shown in Figure 13b. Detachment occurred when the longitudinal destructive force exceeded the kernel's force chain value, disrupting the "arrangement unit" and breaking the longitudinal balance. The threshing trajectory thus followed the axial direction. However, kernel stacking and mutual extrusion constrained the threshing direction, resulting in a lower threshing quantity compared to the transverse process.

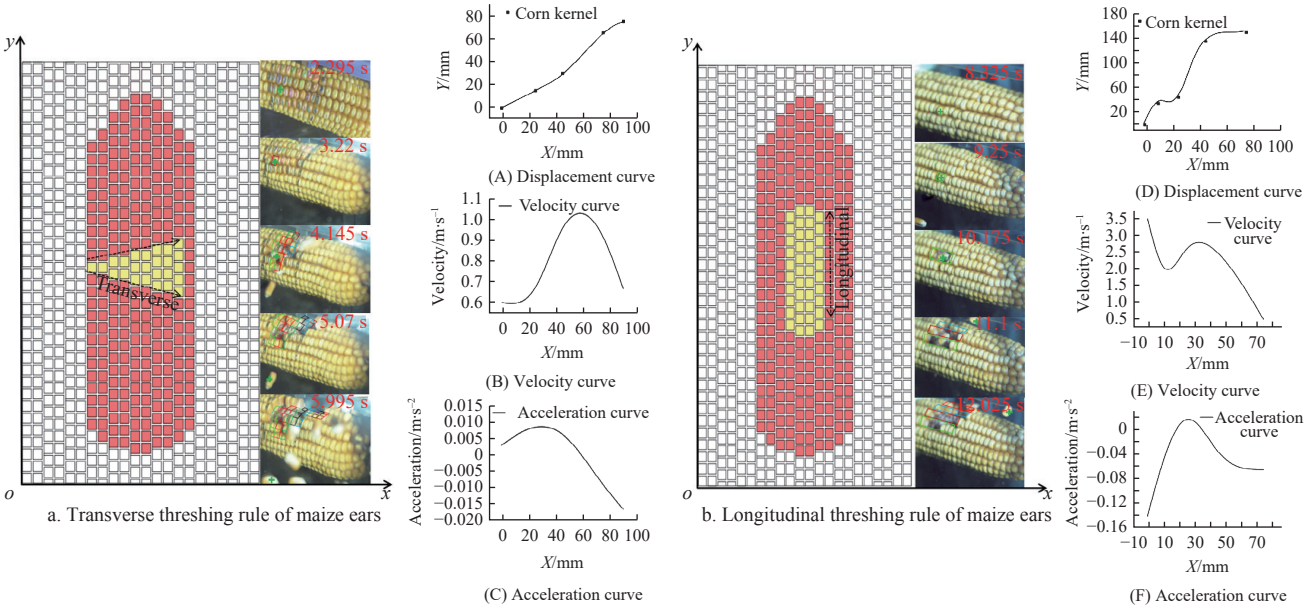

Figure 13 Analysis of maize ear threshing rule

As shown in Figures 10a-10f, the movement trajectories of maize kernels resemble parabolic motion. During threshing, kernel speed gradually decreases under gravity and air resistance. At the trajectory's highest point, only the horizontal velocity component remains, after which kernels undergo gravitational acceleration. Subsequently, when air resistance and kernel weight reach an equilibrium, velocity decreases rapidly with position change, and acceleration diminishes under the ongoing effect of air resistance.

5 Conclusions

1) The contact forces between the large, middle, and small sections of maize ears were defined, and the contact forces in each region were 0.713 N, 0.735 N, and 0.67 N, respectively, indicating that the contact forces were approximately equal and the mean value of the contact force F_c was 0.706 N.

2) Under identical impact angles and ear directions, transverse threshing outperformed longitudinal in both quantity and row number. The three-dimensional force hierarchy (Z>Y>X) identified the Z-direction as the primary component of the impact force, which increased with the impact angle. Furthermore, force values in the same ear direction were highest in the large section, followed by the middle and small sections, with longitudinal forces consistently exceeding transverse values in all regions.

3) The destructive force of the longitudinal force chain network significantly exceeded that of the transverse network. The transverse destructive force was inversely proportional to both the impact angle and the number of threshing rows, whereas the longitudinal force exhibited the opposite relationship with the number of rows. Furthermore, the Z-direction force value was

closely related to the destructive force. It was found that the force chain network, arrangement order, kernel size, and stack number all differentially influenced the airflow change rate in the same area under different maize ear directions.

4) High-speed photography revealed that the transverse threshing process followed the "arrangement unit" along a spiral path around the maize ear circumference, while longitudinal threshing proceeded along the balance force chain in an axial trajectory. The movement trajectories of maize kernels are all similar to parabolic movements.

Acknowledgements

This research was funded by the National Natural Science Foundation of China (Grant No. 52275245) and the Henan Science and Technology Research Program (Grant No. 222103810041). This research can only be done with the help of the postgraduate students in the research team. We are grateful for the support of the fund project and the research team members.

[References]

[1] Zhu X, Chi R J, Ma Y Q. Effects of maize varieties and moisture content on mechanical properties of maize. Agronomy, 2023; 13(2): 545.

[2] Xie R Z, Ming B, Gao S, Wang K R, Hou P, Li S K. Current state and suggestions for mechanical harvesting of maize in China. Journal of Integrative Agriculture, 2022; 21(3): 892–897.

[3] Li X P, Zhang W T, Xu S D, Du Z, Ma Y D, Ma F L, et al. Low-damage maize threshing technology and maize threshing devices: A review of recent developments. Agriculture, 2023; 13(5): 1006.

[4] Xu J, Meng J H, Quackenbush L J. Use of remote sensing to predict the optimal harvest date of maize. Field Crops Research, 2019; 236: 1–13.

[5] Gu R L, Huang R, Jia G Y, Yuan Z P, Ren L S, Li L, et al. Effect of mechanical threshing on damage and vigor of maize seed threshed at different moisture contents. Journal of Integrative Agriculture, 2019; 18(7): 1571–1578.

[6] Feng X, Wang L J, Bi S Y, Wang B, Ma Z, Gao Y. Effects of threshing devices, maize varieties and moisture content of grains on the percentage of maize grains broken in harvesting. Agronomy, 2023; 13(6). DOI: 10.3390/agronomy13061615

[7] Zhang C, Geng D Y, Xu H, Li X, Ming J R, Li D X, et al. Experimental study on the influence of working parameters of centrifugal fan on airflow field in cleaning room. Agriculture, 2023; 13(7). DOI: 10.3390/agriculture13071368

[8] Wang K R, Xie R Z, Ming B, Hou P, Xue J, Li S K. Review of combine harvester losses for maize and influencing factors. Int J Agric & Biol Eng, 2021; 14(1): 1–10.

[9] Ma Z, Han M, Li Y M, Yu S C, Qian D A, Chandio F A. Comparing kernel damage of different threshing components using high-speed cameras. Int J Agric & Biol Eng, 2020; 13(6): 215–219.

[10] Wang Y Z, Li L L, Gao S, Guo Y N, Zhang G Q, Ming B, et al. Evaluation of grain breakage sensitivity of maize varieties mechanically-harvested by combine harvester. Int J Agric & Biol Eng, 2020; 13(5): 8–16.

[11] Dong W X, Wu Y S, Liu F, Hu H T, Yan J G, Bai H B, et al. Design and experiment of a harvesting header for wide-narrow-row maize. Applied Sciences-Basel, 2024; 14(3): 14.

[12] Fu Q K, Fu J, Chen Z, Cui S B, Ren L Q. Experimental study on lodged maize harvest loss of small harvesters. Int J Agric & Biol Eng, 2022; 15(4): 123–129.

[13] Zhang Z L, Geng A J. Development and evaluation of low-damage maize snapping mechanism based on deformation energy conversion. Applied Sciences-Basel, 2021; 11(24): 17.

[14] Basuki M, Aprilyanti S, Azhari, Madagaskar. Design of maize thresher. Journal of Physics. Conference Series, 2020; 1500(1). DOI: 10.1088/1742-6596/1500/1/012075

[15] Yang L, Cui T, Qu Z, Li K H, Yin X W, Han D D, et al. Development and application of mechanized maize harvesters. Int J Agric & Biol Eng, 2016; 9(3): 15–28.

[16] Fu J, Chen Z, Han L J, Ren L Q. Review of grain threshing theory and technology. Int J Agric & Biol Eng, 2018; 11(3): 12–20.

[17] Hussain S Z, Naik H R, Rather A H, Khan J. Comparative evaluation of horizontal maize cob sheller with traditional methods of maize shelling. Research on Crops, 2009; 10(1): 168–170.

[18] Wang X F, Wang Y J, Zhao H B, Tao H T, Gao W, Wu Z Z, et al. Influence of hot-air drying on the starch structure and physicochemical properties of two maize cultivars cultivated in East China. Journal of Cereal Science, 2023; 114: 103796.

[19] Ghafori H, Hemmat A, Borghaee A M, Minaei S. Physical properties and conveying characteristics of maize and barley seeds using a suction-type pneumatic conveying system. African Journal of Agricultural Research, 2011; 6(27): 5972–5977.

[20] Zhang C L, Zhang X Y, Zheng Z H, Xie X D, Liu L C, Chen L Q. Numerical simulation and test of the disturbance air suction garlic seed metering device. Machines, 2022; 10(12): 1127.

[21] Zhao J L, Zhao H N, Tang H, Wang X G, Yu Y J. Bionic threshing component optimized based on MBD-DEM coupling simulation significantly improves maize kernel harvesting rate. Computers and Electronics in Agriculture, 2023; 212: 108075.

[22] Zhang H M, Chen B, Li Z J, Zhu C H, Jin E, Qu Z. Design and simulation analysis of a reverse flexible harvesting device for fresh maize. Agriculture, 2022; 12(11): 1953.

[23] Yang F, Du Y F, Fu Q F, Li X Y, Li Z, Mao E R, et al. Design and testing of seed maize ear peeling roller based on Hertz theory. Biosystems Engineering, 2021; 202: 165–178.

[24] Dong J Q, Zhang D X, Yang L, Cui T, Zhang K L, He X T, et al. Discrete element method optimisation of threshing components to reduce maize kernel damage at high moisture content. Biosystems Engineering, 2023; 233: 221–240.

[25] Steponavičius D, Pužauskas E, Špokas L, Jotautienė E, Kemzūraitė A, Petkevičius S. Concave design for high-moisture maize ear threshing. Mechanics, 2018; 24(1): 80–91.

[26] Zhang K, Cao S K, Chen X S, Cao C, Wu C Z. Design of longitudinal axial flow threshing and separating device of maize grain combine harvester. Applied Mechanics and Materials, 2017; 863: 251–254.

[27] Bakharev D, Pastukhov A, Volvak S, Kovalev S. Study of seed maize threshing process. Proceedings of the 19th International Scientific Conference Engineering for Rural Development, 2020.

[28] Fernando S D, Hanna M A. Design and development of a threshing chamber and pneumatic conveying and cleaning units for soybean harvesting. Transactions of the ASAE, 2005; 48(5): 1681–1688.

[29] Pastukhov A G, Bakharev D N, Parnikova T V. Differentiated threshing of seed maize with minimal grain crushing. IOP Conference Series: Earth and Environmental Science, 2021; 659(1): 012095.

[30] Li X P, Li Y N, Peng B, Xu S D, Wang J Y, Sun R Z, et al. Characteristics and numerical simulation of maize ear threshing under mixed airflow. Int J Agric & Biol Eng, 2025; 18(3): 278–288.

[31] Li X P, Wang J Y, Li Y N, Xu S D, Hou J R. Fracture regularity of maize kernel and stalk based on fractal theory. Int J Agric & Biol Eng, 2025; 18(3): 37–43.

[32] Li X P, Wu K, Jin X, Gao C Y, Gao L X. Analysis on discrete process of kernels caused by beak pecking maize ear by simulating threshing. Transactions of the CSAE, 2015; 31(18): 34–40.

[33] Li X P, Ma L, Geng L X, Wang S S, Pang J, Ji J T. Performance test and parameter optimization of maize seed bionic thresher. Transactions of the CSAE, 2017; 33(5): 62–69.

[34] Li X P, Zhang W T, Xu S D, Ma F L, Du Z, Ma Y D, et al. Calibration of collision recovery coefficient of maize seeds based on high-speed photography and sound waveform analysis. Agriculture, 2023; 13(9). DOI: 10.3390/agriculture13091677